A Triple-Layer Electromagnetic Heat Exchanger With Plane Poiseuille Flow: Control and Local Onset of Thermal Runaway

Ajit A. Mohekar [ORCID], Burt S. Tilley [ORCID], and Vadim V. Yakovlev [ORCID], *Senior Member, IEEE*

Abstract—An electromagnetic (EM) heat exchanger (HX) is a device which converts EM energy into a usable form of heat. In this article, we present a 2-D multiphysics model mimicking the operation of a layered EM HX and simulating the nonlinear interaction between EM wave propagation, energy transport, and fluid flow. A triple-layer geometry of the EM HX represents a lossy ceramic slab surrounded by two channels with a plane Poiseuille flow of a lossless coolant. Validation of the model developed in COMSOL Multiphysics is done by comparing the results with the output of another numerical model, which uses a second-order implicit–explicit scheme where advective and diffusive terms are treated implicitly and the nonlinear heat source is treated explicitly. Layer thicknesses are chosen such that an electric field resonance is achieved in the central layer. Because of the resonance, a power response curve is found to be a double S-curve. We show that EM HXs operating on the middle branch of the double S-curve are favorable and efficient compared to the those operating on the lower or upper branch. Careful examination of transient evolution of temperature confirms that thermal runaway occurs when the local maximum temperature reaches a critical value. The model predicts a hotspot in ceramic region when thermal runaway initiated locally. We generate power response curves for increasing Péclet numbers, which is defined as the ratio of heat convection to conduction within the fluid region, and show that temperatures of upper and middle branches keep dropping with Péclet numbers.

Index Terms—Electromagnetic (EM) heat exchanger (HX), hotspots, microwave heating, multiphysics modeling, thermal runway.

I. INTRODUCTION

TRADITIONAL electromagnetic (EM) heating applications include thermal processing of food products, microwave-assisted chemistry, and high-temperature treatment of materials [1]–[6]. Currently under development are high-power EM heat exchangers (HX) for power beaming applications. The uses of EM HX include thermal thrusters employing EM energy to produce thrust by thermal expansion of a compressed gas [7], beamed energy propulsion [8], [9], solar thermal collectors [10], and wireless energy transfer [11]–[19].

Microwaves (MW) and millimeter waves (MMW) are a promising choice in continuous power-beaming applications as they are readily available at high power. While MMW may have advantages over MW in terms of dimensions of transmitting antennas, they may not efficiently propagate through the atmosphere [11], [13]. Depending on efficiency of transmission, MMW may be preferable at high altitudes or in space, and MW or near MMW may be convenient for ground-to-ground power beaming. For the latter, one of the critical components is a robust EM HX which efficiently converts EM energy into heat.

Heat generation in lossy materials irradiated by EM waves depends on the loss factor which can be seen as representation of both electrical conductivity and dielectric losses. When the electric field propagates through a material with a nonzero loss factor, its amplitude decays due to the EM losses. This lost energy is converted into heat, resulting in a temperature rise. For many ceramic materials, including zirconia or silicon carbide, the loss factor can be modelled with an exponential fit in temperature [20], [21]. One peculiar phenomenon associated with EM thermal processing of such materials is *thermal runaway*, a nonlinear phenomenon in which a small increase in the applied EM power invokes a sharp temporal increase in temperature. Thermal runaway was studied experimentally [22], [23] and computationally [21]. These works show that temperature during thermal runaway increases rapidly as the maximum temperature in processed material reaches a critical value. Temperatures during thermal runaway are high enough to cause material damage through melting or cracking.

Analytical models of EM heating of a single dielectric slab [24] and a three-layer structure (Fig. 1) [25] describe thermal runway. Both the models describe equilibrium of EM heating by a parametric plot of average steady temperatures as a function of applied power that is called a *power response curve*. These models consider uniform heating of thin laminate structures which are irradiated by symmetric EM plane waves normal to the laminate surface. In these models, the wavelength of the incident EM waves is assumed to be much longer than the layer thickness. The resulting power response curve in this case is an S-curve as
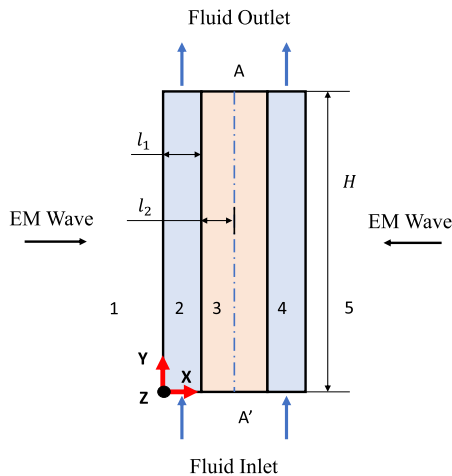
Fig. 1.   Geometry of the three-layered system subjected to EM heating (symmetric about AA'). Media 1 and 5 are free space, layers 2 and 4 are lossless fluid, and layer 3 is a lossy dielectric.

shown in Fig. 2(a). A branch of the power response curve is stable (or unstable) when its slope is positive (or negative) [25]. Generally speaking, an S-shaped power response curve has two stable branches: one at lower and one at higher temperatures. EM HXs operating on the lower stable temperature branch may not operate efficiently. On the other hand, high-stable temperatures may damage the ceramic material itself.

Recently, an analytical model [26], [27] studying EM heating of thin triple-layer laminate (lossless–lossy–lossless, Fig. 1) has suggested an innovative electric-field-resonance-based approach to control thermal runway. Similar to [24] and [25], these models consider uniform heating by symmetric normal plane wave irradiation. When wavelength of the incident wave is comparable to the layer's thickness, an electric field resonance may be achieved in the central layer. The response curve in this case acquires a middle stable branch and becomes a double S-curve as shown in Fig. 2(b). The model [26] first proved the existence of the double S-curve and extended model [27] confirmed that the field resonance in the lossy layer causes the response curve to have a middle stable branch. The model described in [16] numerically verifies existence of a double S-curve for a triple-layer laminate structure. The electric field resonance can be also achieved in a two layer (lossless–lossy) laminate undergoing nonsymmetric normal excitation by EM waves [18]. The implication from these models is that when an EM HX operates on the middle branch, stable temperatures are elevated, but remain below values where mechanical damage to the material can occur. This opens up a window to investigate how EM HX could efficiently operate on the middle branch.

The working principle of a high-power EM HX is based on interactions between EM wave propagation, internal energy conservation, and fluid mass and momentum conservation, so the design of a practical device requires particularly extensive experimentation. Computational models can help identify the competing mechanisms in the energy balances, leading to potential insight on how this phenomena can be controlled. While asymptotic models are helpful in identifying the mechanisms
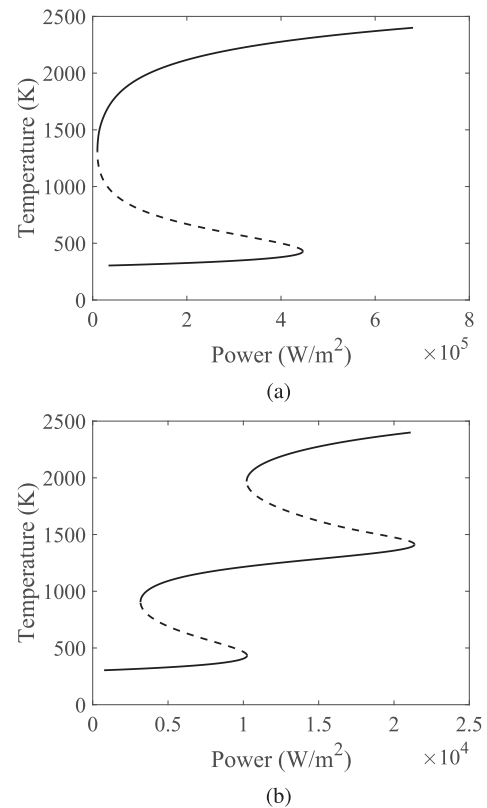
Fig. 2.   Power response curves for a triple-layer laminate (lossless–lossy–lossless, Fig. 1) structure. (a) S-curve (no electric field resonance) as in [24] and (b) a double S-curve (electric field resonance in the lossy layer) [26], [27]. Both curves are obtained using the model [26], [27] for material parameters of zirconia in region 3 and of 50% glycerin solution in regions 2 and 4. Solid and dashed lines represent stable and unstable solutions, respectively.

leading to a net energy balance [26], [27], computational techniques are needed to understand how local phenomena can instigate large changes in temperature.

The goal in this article is to extend the model in [16] to describe situations where the the heat losses to the environment from the system, the power delivered to the system, and the convective transport of energy are larger than the cases explored in [16]. The model in [16] is validated in the limit when each of these powers were small. We consider a triple-layered structure (Fig. 1) in which a lossy ceramic (region 3) is surrounded by lossless coolant channels (regions 2 and 4). Ceramic region is heated by EM waves and coolant extracts energy from the heated region through conduction and convection. We describe a model developed in COMSOL Multiphysics and incorporate coupling between electromagnetic, fluid flow, and heat transfer phenomena by introducing a fully developed plane Poiseuille fluid flow in regions 2 and 4 along the positive Y-axis. In order to validate the COMSOL model, we compare the results with the ones produced by another numerical model developed using a two-step second-order implicit–explicit (IMEX) finite difference scheme [28] where linear terms are treated implicitly and nonlinear terms are treated explicitly. We first consider the case with no fluid flow and visualize steady-state profiles of temperature and electric field. Then we introduce fluid flow in

TABLE I
CONSIDERED MATERIAL PROPERTIES FOR SIMULATIONS

Region	ϵ_{r_j}	$\sigma_j(T)[\frac{S}{m}]$	$\rho_j[\frac{kg}{m^3}]$	$c_{p_j}[\frac{J}{kgK}]$	$\mu_j[\frac{Ns}{m^2}]$	$k_j[\frac{W}{mK}]$
$j = 1, 5$	1	0	-	-	-	-
$j = 2, 4$ [29], [30]	45	0	1248	2405	0.004	0.4
$j = 3$ [21]	6.69	$0.0004e^{2.32T}$	2848	217	-	0.2

regions 2 and 4 by maintaining nonzero pressure drop across the inlet and outlet. When fluid flow is present, the EM losses in the ceramic are balanced by power absorbed by the fluid and external heat losses to the surrounding. The Biot number characterizes thermal losses to the environment. Previous studies [26], [27] have shown that the response curves usually retains the typical double S shape when the Biot number is varied. One of the goals of this article is to investigate how convection heat transport affects the shape of the response curve. The amount of heat carried away by the fluid is characterized by the Péclet number, which is the ratio of thermal energy convected to the fluid to the thermal energy conducted within the fluid. We generate power response curves for different Péclet numbers, and discuss how convection affects the shape of response curves. We then determine effectiveness of the energy absorption by the fluid by calculating the overall thermal efficiency of the considered EM HX and show how higher efficiencies can be achieved along with having control over thermal runaway.

The electric field resonance in the lossy layer, which is required for the existence of the middle branch, is dependent on permittivities of fluid and ceramic regions [26], [27]. Another goal of this article is to investigate cases where resonance criteria is not followed exactly, and to determine how sensitive is the middle branch to the permittivity variations.

II. DEVELOPMENT OF NUMERICAL MODELS

We consider plane EM waves incident from both sides with the assumption that incoming waves are polarized along the *Z*-direction and traveling in the *X*-direction. The time-averaged power density of the incident plane wave is

$$P_{av} = \frac{E_0^2}{2\psi} \quad (1)$$

where E_0 is the strength of incident electric field, and ψ is characteristic impedance of free space. In order to achieve an electric field resonance necessary to produce the double S-curve, we need to satisfy following conditions [26]:

$$l_1 = \frac{n_1\lambda_2}{4} \quad l_2 = \frac{n_2\lambda_3}{4} \quad (2)$$

where l_1 and l_2 are thicknesses of regions 2 and 3. n_1 and n_2 are any odd integers, and λ_2 and λ_3 are wavelengths in regions 2 and 3, respectively. In all of our simulations presented in the article, we take $n_1 = 1$, $n_2 = 3$, and $H = 20l_2$.

A. Assumptions and Material Properties

An incompressible and viscous fluid in region 2 is composed of equal parts glycerin and water. The frequency f of incident EM waves is assumed to be 2.45 GHz. Dielectric and thermal properties of glycerin are taken from [29] and [30], respectively. Region 3 is a lossy zirconia; its material properties are borrowed from [21]. A full exploration of the temperature-dependent material properties is beyond the scope of this article. However, the electric field resonance, which is essential for the existence of the middle branch, is particularly sensitive to temperature variations in the permittivity. As a leading-order approximation, we determine intervals about the reference permittivity over which the double S curve would exist. We think this gives insights on the impact of variable permittivity on this phenomenon, while providing a tractable problem to address. All the materials used are assumed nonmagnetic ($\mu_r = 1$). In addition, only the material in the middle layer (region 3) absorbs MW energy, and the outer layers (regions 1, 2, 4, and 5) are considered lossless. Material properties considered in this article are summarized in Table I.

B. Governing Equation

Since the plane waves are polarized along the *Z*-direction, Maxwell's equations governing electric field in both regions reduce to Helmholtz's equations. We scale electric field with E_0. Lengths along the *X*-direction in regions 2 and 3 shown in Fig. 1 are scaled with l_1. Lengths along the *Y*-direction in both regions are scaled with H. The nondimensional temperature is given as $T_j = \frac{\bar{T}_j - T_A}{T_A}$, where T_j and $\bar{T}_j$ are scaled deviation temperatures from ambient and dimensional temperatures in regions $j = 1$ and 2, respectively, and T_A is ambient temperature. In our models, T_A is set at $300\,K$. Time is scaled on the conduction time scale in region 3 as $\frac{l_2^2}{\alpha_3}$, where $\alpha_j = \frac{k_j}{\rho_j c_{p_j}}$ is thermal diffusivity, k_j is thermal conductivity, ρ_j is density, and c_{p_j} is specific heat of the respective regions 2 and 3. Finally, the velocity of fluid is scaled with $\bar{V}$, where $\bar{V} = \frac{|P_g|l_1^2}{2\mu}$, $|P_g|$ is the magnitude of pressure gradient maintained across the inlet and outlet. The resulting set of nondimensional governing equations for the electric field amplitude and the energy balances in regions 2 and 3 is

$$\frac{\partial^2 E_2}{\partial x^2} + \eta^2 \frac{\partial^2 E_2}{\partial y^2} + \gamma_2^2 E_2 = 0 \quad (3)$$

$$\frac{\partial^2 E_3}{\partial x^2} + \eta^2 \frac{\partial^2 E_3}{\partial y^2} + \gamma_3^2 E_3 = 0 \quad (4)$$

$$\frac{\partial T_2}{\partial t} + \eta\alpha Pe\left(v\frac{\partial T_2}{\partial y}\right) = \alpha\left[\frac{\partial^2 T_2}{\partial x^2} + \eta^2\frac{\partial^2 T_2}{\partial y^2}\right] \quad (5)$$

$$\frac{\partial T_3}{\partial t} = \frac{\partial^2 T_3}{\partial x^2} + \eta^2\frac{\partial^2 T_3}{\partial y^2} + P|E_3|^2\sigma_3(T_3) \quad (6)$$

where E_2 and E_3 are nondimensional electric field strengths in region 2 and 3, respectively, $\eta = \frac{l_1}{H}$, $\gamma_2^2 = k_0^2\epsilon_{r_2}$, and $\gamma_3^2 =$

$k_0^2[\epsilon_{r_3} + i\frac{\sigma_3(T_3)}{\omega\epsilon_0}]$ are nondimensional wavenumbers, $k_0 = \frac{\omega}{c}l_1$ is the nondimensional wavenumber of free space, ω is angular frequency, c is the speed of EM wave in free space, ϵ_0 is permittivity of free space, ϵ_{r_2} and ϵ_{r_3} are relative permittivities of regions 2 and 3, respectively, T is temperature, $\sigma_3(T)$ is temperature-dependent electrical conductivity, $\alpha = \frac{\alpha_2}{\alpha_3}$, $Pe = \frac{l_1\bar{V}}{\alpha_2}$ is the Péclet number, v is the nondimensional fluid velocity along the positive Y-direction, and nondimensional power $P = \frac{1}{2}\frac{E_0^2\omega\epsilon_0 l_1^2}{k_3 T_A}$.

Since our focus in this article is on the coupling between the field strength and temperature, we chose an exact laminar solution to the Navier–Stokes equations; fully developed plane Poiseuille fluid flow is given by the equation

$$v(x) = -(x^2 - x) \tag{7}$$

Although this assumption is limited in terms of the Reynolds number of the flow, our formulation is amenable for larger Reynolds numbers if we include Taylor dispersion for sufficiently long channels [31].

C. Boundary Conditions

As region 1 is free space, for $x < 0$

$$E_1(x) = e^{ik_0 x} + \tau e^{-ik_0 x} \tag{8}$$

where E_1 is the electric field in region 1, τ is the reflection coefficient between regions 1 and 2. At the left boundary between regions 1 and 2, τ can be eliminated by applying continuity of the electric and magnetic fields [24], which yields

$$\frac{\partial E_2}{\partial x} + ik_0 E_2 = 2ik_0. \tag{9}$$

Similarly, at the interface between regions 2 and 3

$$E_2 = E_3$$
$$\frac{\partial E_2}{\partial x} = \frac{\partial E_3}{\partial x}. \tag{10}$$

Since a symmetry condition is assumed at AA', we have

$$\frac{\partial E_3}{\partial x} = 0. \tag{11}$$

At the top and bottom boundaries, we apply

$$\frac{\partial E_2}{\partial y} = \frac{\partial E_3}{\partial y} = 0. \tag{12}$$

For the energy equations (4) and (5), at the left boundary between regions 1 and 2 we have convective losses to the surroundings characterized by Newton's law of cooling as

$$k\frac{\partial T_2}{\partial x} = Bi T_2 \tag{13}$$

where $k = \frac{k_2}{k_3}$, $Bi = \frac{hl_1}{k_3}$ is the Biot number, h is the heat transfer coefficient, and k_j is the thermal conductivity of region j. In our simulations presented in this article, we specify $h = 5\,W/m^2 K$. At the interface between regions 2 and 3, we assume perfect thermal contact

$$T_2 = T_3$$
$$k\frac{\partial T_2}{\partial x} = \frac{\partial T_3}{\partial x}. \tag{14}$$

At the line of symmetry AA'

$$\frac{\partial T_3}{\partial x} = 0. \tag{15}$$

Top boundaries in regions 2 and 3 are insulated, so that

$$\frac{\partial T_2}{\partial y} = \frac{\partial T_3}{\partial y} = 0. \tag{16}$$

The lower boundary at $y = 0$ is maintained at the fixed ambient temperature in regions 2 and 3

$$T_2 = T_3 = 0. \tag{17}$$

We develop two models to solve the system (3)–(7). One is with a finite-difference scheme implemented in MATLAB, the other is with finite-element method (FEM) in COMSOL Multiphysics. We consider two different cases: the first is with no fluid flow, i.e, $Pe = 0$, and the second with fluid flow $Pe \neq 0$. In both cases, we compare steady-state temperature profiles produced by both the numerical models.

D. Finite-Difference Model

The finite-difference scheme presented here is second order both in time and space. Spatial derivatives of electric field in (3) and (4) are discretized using second-order central difference scheme. The final pentagonal linear system of equations is solved using GMRES solver [32]. Energy equations in both regions are then solved using a two-step alternating-direction IMEX method [28]. The nonlinear heat source in region 3 is treated explicitly and the rest of the terms are treated implicitly. At each step we solve the system of linear equations using a standard tridiagonal solver [33]. The external boundary and interface conditions involving derivatives are discretized with central differencing with the ghost points method [34].

Due to explicit treatment of the nonlinear heat source, the method is unstable for larger time steps. After carrying out numerical experiments, we find temporal step size 0.1 is sufficient when there is no thermal runaway, and when it is expected, we choose 0.01 as step size when discretizing time derivatives. Section of spatial step size is based on Nyquist criterion [35]

$$S_j < \frac{\lambda_j}{2} \tag{18}$$

where S_j is the maximum size of the cells. According to (18), the step size in both the X- and Y-directions should be such that we have at least 2 cells per wavelength in both regions. As a general rule for solving Helmholtz equations, 10 to 12 grid points per wavelength are sufficient for producing reasonable accuracy at smaller wavenumbers [36]. With this consideration, we discretize each region such that we have 61 uniformly distributed grid points along the X- and Y-directions. In other words, we choose approximately 66 and 10 cells per wavelength along the X and Y-directions. In addition, convergence tests are
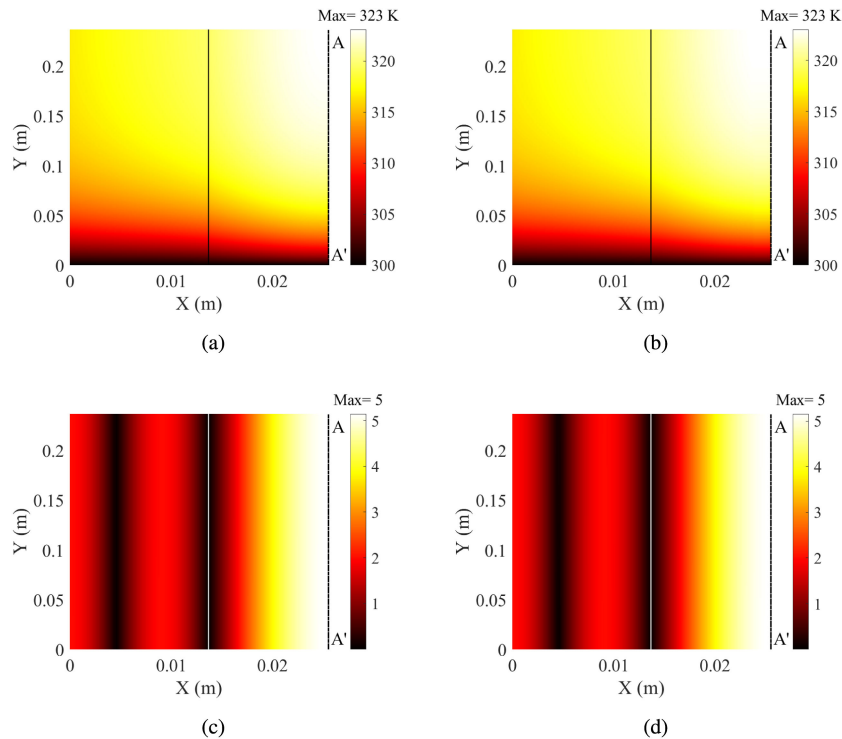
Fig. 3. Steady-state dimensional T profiles produced by (a) IMEX and (b) COMSOL, dimensionless $|E|$ profiles given by (c) IMEX and (d) COMSOL models for power $P_{av} = 3000$ W/m^2 with no flow case $Pe = 0$. The solid line represents the interface between regions 2 and 3 and AA' is the axis of symmetry. Maximum and average E_r in comparison of (a) and (b) is 0.005 and 6.57×10^{-4}, and between (c) and (d) is 0.24 and 0.004, respectively.

carried to determine number of grid points in each region. We find that change in average and maximum T and $|E|$ is below 10^{-2} when grid points in each region increased from 51 to 61.

E. COMSOL Multiphysics Model

The geometry is discretized using cubic Lagrange triangular elements. In [16], [37], and [38], the maximum element size is chosen such that we have at least 15 elements per wavelength throughout the computational domain. To determine the mesh size, we again carried out converge tests and throughout the computations below, we discretize both the domains with approximately 25 elements per wavelength.

As the problem is highly nonlinear due to temperature dependent electrical conductivity, we solve energy equations using COMSOL's time-dependent solver along with a time-stepping algorithm provided in COMSOL package. The solver discretizes time using the second-order implicit backward-difference formula. The time step taken by the solver is adjusted depending on temporal gradients of the fields. Finally, the steady state is assumed to be reached when absolute difference between average temperatures at previous and current time steps falls below 10^{-6}. COMSOL Multiphysics 5.3a package runs on a server which has two Intel Xeon CPU E5-2643 processors and 128 GB of installed RAM. Typical time taken for a simulation to perform is about 10 min.

III. RESULTS

First, we compare the steady-state temperature and electric field profiles produced by both COMSOL Multiphysics and

IMEX models. The comparison is made for two cases; one with no fluid flow and another with fluid flow. As both models use different discretization schemes, the results from the COMSOL model are interpolated onto the grid used in the IMEX model using MATLAB's Delaunay triangulation technique. We quantify the differences seen in the profiles using

$$E_r = \left| \frac{\phi_{IMEX} - \phi_{COMSOL}}{\phi_{IMEX}} \right| \qquad (19)$$

where E_r is the absolute relative error which also includes interpolation error, and ϕ can be T or $|E|$. We then use the COMSOL model to produce power responses for different Pe.

A. No Fluid Flow ($Pe = 0$)

We set $Pe = 0$ and solve the system (3)–(7) along with the boundary conditions (10)–(17) in COMSOL Multiphysics and with the IMEX scheme. For this case, the steady state is achieved when EM losses are balanced by thermal losses to the surroundings.

Fig. 3 shows the comparison of steady-state temperature and electric field profiles in regions 2 and 3 for incident power of $P_{av} = 3000$ W/m^2. Power response curves for different Pe are shown in Fig. 4. Stable branches shown in this plot are produced by performing parametric sweep on incident powers with different initial temperatures, and average steady-state temperatures are plotted against the incident power. It is seen that lower, middle, and upper branches are achieved when initial temperatures are maintained at 300, 1000, and 2500 K, respectively. For $P_{av} = 3000$ W/m^2, the steady-state temperatures are low
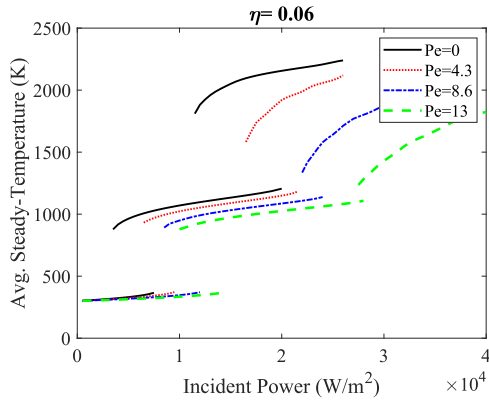
Fig. 4.   Stable branches of power response curves for $\eta = 0.06$ and different Péclet numbers produced using COMSOL Multiphysics model.

(Fig. 3) and EM HX operates on the lower branch which can be seen from Fig. 4. In Fig. 5, as we increase the P_{av} to 8000 W/m^2, we observe significant rise in temperature: Maximum value in ceramic region increases from 323 to 1400 K, and solution is found to be on the middle branch (see Fig. 4). As a result of this transition from lower to middle branch, a hotspot is observed in the lossy region which indicates localized heating. We discuss this phenomenon in following section.

As soon as we achieve transition between lower and the middle branch, we observe nonuniform distribution of electric field amplitude as seen in Figs. 3 and 5. When the device operates on the lower branch for $P_{av} = 3000$ W/m^2 and $Pe = 0$, temperatures are low (maximum of 323 K) and $\sigma_3 \sim 0.0004$ S/m, therefore, attenuation of electric field amplitude in ceramic region is small as seen in Fig. 3 (c) and (d). On the other hand, when $P_{av} = 8000$ W/m^2 for $Pe = 0$, we operate on the middle branch and average temperatures are high (maximum of 1400 K). Dirichlet condition maintained at the bottom boundary causes a nonuniform temperature distribution, and σ_3 is maximum (or minimum) where temperature is maximum (or minimum), therefore, it is expected to see attenuation of field amplitude in high-temperature regions, which is seen in Fig. 5 (c) and (d) where maximum field amplitude is observed near the bottom boundary where the temperature is minimum.

B. Fluid Flow ($Pe \neq 0$)

We now introduce fluid flow along the positive *Y*-direction in region 2. As the fluid is forced to move in region 2, it collects thermal energy from the heated region 3 through conduction and convection. The rate at which fluid delivers the energy at the outlet (in W/m^2) is given by

$$P_{abs} = \frac{k_2 T_A}{l_1} Pe \int_0^1 T_o v_o dx \qquad (20)$$

where T_o and v_o are temperature and fluid velocity profiles at the outlet, respectively. For $Pe \neq 0$, the EM losses in the ceramic are balanced by P_{abs} and thermal losses to the surrounding. Overall efficiency of the device can be defined as the ratio of thermal

power delivered by the fluid at the outlet to incident power of EM waves. Using the expression above, we calculate the overall thermal efficiency of the power absorption χ as

$$\chi = \frac{P_{abs} l_1}{P_{in} H} \times 100 \ (\%). \qquad (21)$$

1) $Pe \sim o(1)$ and $\eta = 0.06$: We now choose velocity scales such that $Pe \sim o(1)$ for $\eta = 0.06$. Physically, fluid is moving slowly in region 2 such that velocities are $o(10^{-5}) \frac{m}{s}$. As P_{abs} increases with Pe, we expect that more power of incident wave would be required to achieve transition from lower branch to the middle one when Pe is increased. This can be confirmed from Fig. 6, where we see that for incident power of 8000 W/m^2 and $Pe = 8.6$, EM HX operates on the lower branch (see Fig. 4) unlike what was seen in Fig. 5. From Fig. 7, when incident power is 15 000 W/m^2, it appears that EM HX operates on the middle branch, and we observe significant rise in temperature at the fluid outlet (from ~ 350 to ~ 1100 K). This suggests that EM HX operating on the middle branch may be more efficient compared to the ones operating on lower branch. We now calculate χ when device is operated on lower, middle, and upper branches for $Pe = 4$, and plot χ as a function of P_{av} in Fig. 8. Although, for $Pe = 4$, average fluid temperatures when the device operates on the upper branch are much higher (~ 2500 K) compared to cases when it operates on the middle branch (~ 1000 K), the middle branch is found to be more efficient for P_{av} between $5800 - 6300$ W/m^2. This plot demonstrates how the devices operated on the middle branch can operate efficiently even when average temperatures are moderate (~ 1000 K).

We extend the COMSOL model and generate stable branches of power response curves for different Pe. The presented model applies the method of resonance-based control over thermal runaway proposed in [26] and [27] to a triple-layer EM HX with plane Poiseuille flow. The stable branches of double S-curves shown in Fig. 4 confirm the existence of the middle branches for low Pe. When the transition between lower and middle branches is achieved, thermal runaway initiates locally but stabilizes on the middle branch where average temperatures are around 1100 K.

We also see from Fig. 4 that average temperatures of upper and middle stable branches keep dropping as Pe is increased. Especially, the upper branches undergo drastic reduction in temperatures compared to the middle and lower branches. This behavior seems plausible because at higher Pe flow speed is high and the rate at which fluid extracts heat from the heated ceramic is large as seen from (20). In general, the amount of heat transfer through convection between coolant and a heated region depends on the temperature difference between them. Convection is large when temperature difference is large. When EM HX operates on the upper branch, there naturally exists a large temperature difference between the coolant and ceramic compared to when EM HX is on middle or lower branch. As a result, the convection heat transfer between the coolant and ceramic is large. In Fig. 9, we plot χ as a function of Pe for $P_{av} = 15\,000$ W/m^2 and $P_{av} = 30000$ W/m^2. Parameter P_{av} is chosen such that steady-state solution is on the middle or
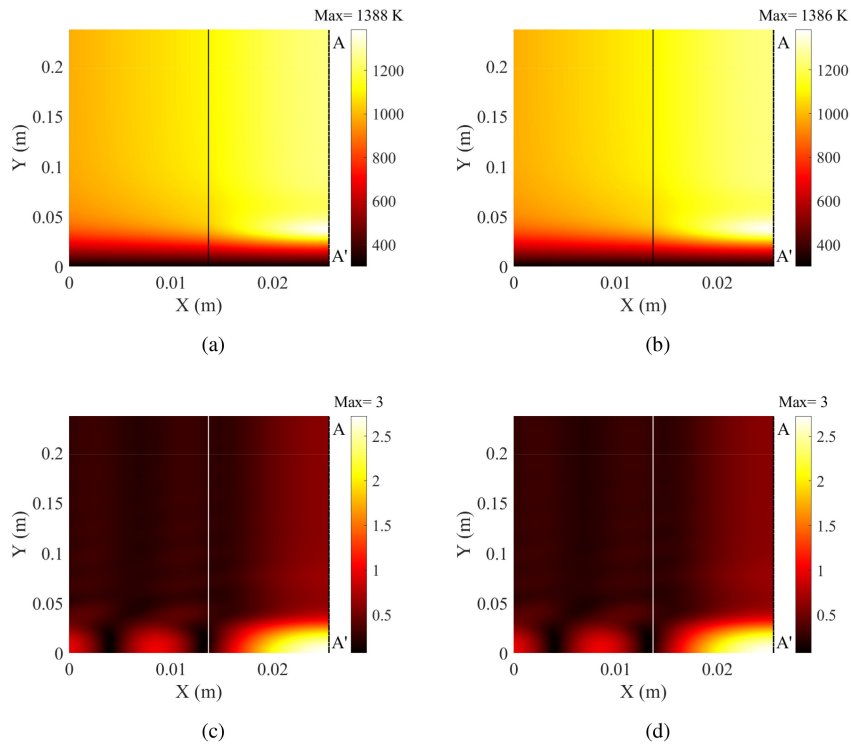
Fig. 5. Steady-state dimensional T profiles produced by (a) IMEX and (b) COMSOL dimensionless $|E|$ profiles given by (c) IMEX and (d) COMSOL models for power $P_{av} = 8000$ W/m^2 with no flow case $Pe = 0$. The solid line represents the interface between regions 2 and 3 and AA' is the axis of symmetry. Maximum and average E_r in comparison of (a) and (b) is 0.01 and 5.3×10^{-4}, and between (c) and (d) is 0.14 and 0.01, respectively.
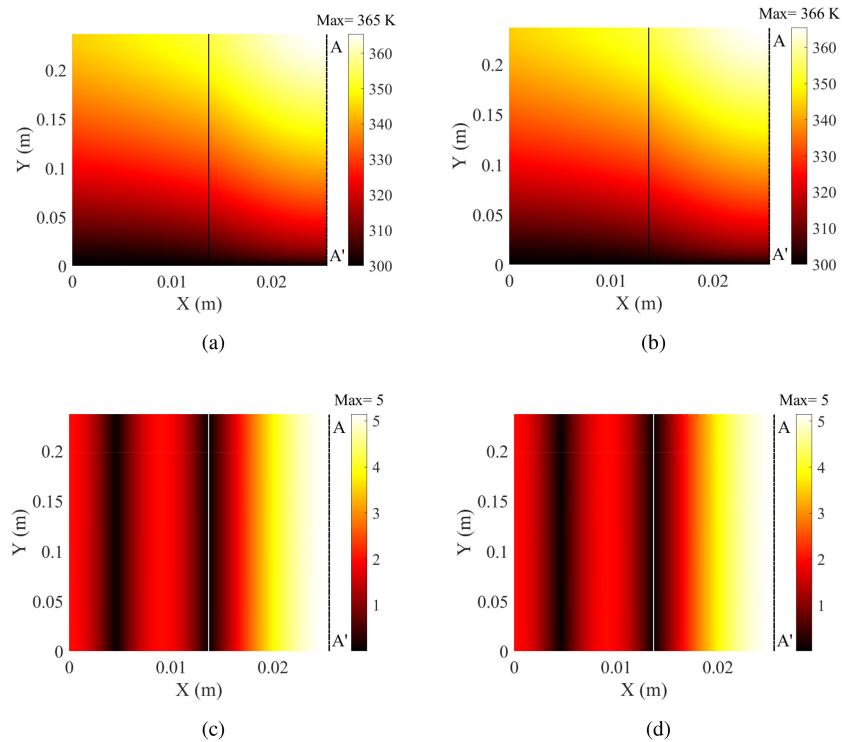
Fig. 6. Steady-state dimensional T profiles produced by (a) IMEX and (b) COMSOL, dimensionless $|E|$ profiles given by IMEX (c) and COMSOL (d) models for power $P_{av} = 8000$ W/m^2 with flow case $Pe = 8.6$ and $\eta = 0.06$. The solid line represents the interface between regions 2 and 3 and AA' is the axis of symmetry. Maximum and average E_r in comparison of (a) and (b) is 0.003 and 1.42×10^{-4}, and between (c) and (d) is 0.24 and 0.004, respectively.
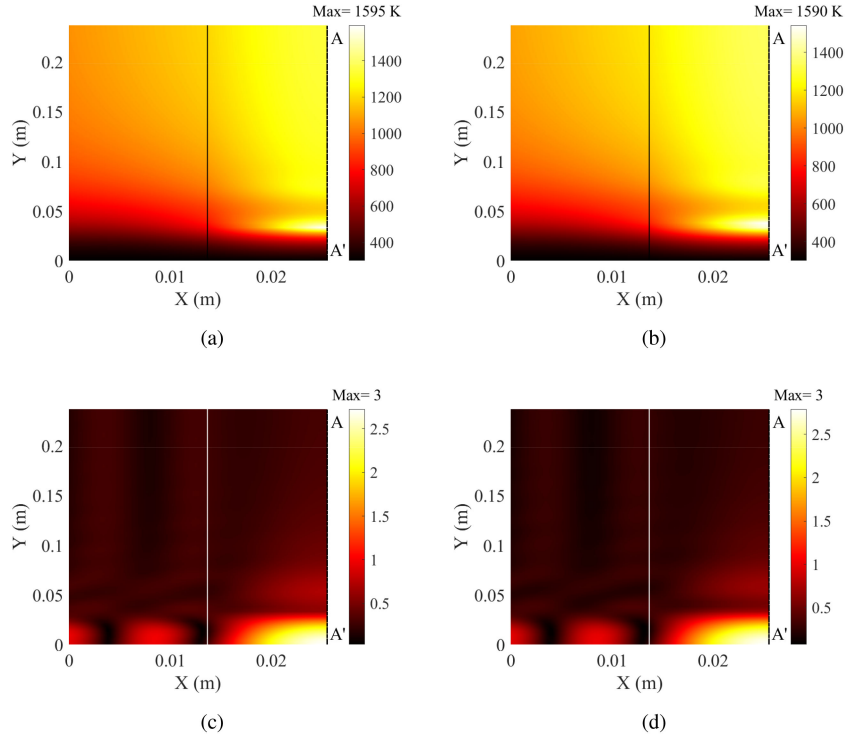
Fig. 7. Steady-state dimensional T profiles produced by (a) IMEX and (b) COMSOL, dimensionless $|E|$ profiles given by (c) IMEX and (d) COMSOL models for power $P_{av} = 15\,000$ W/m^2 with flow case $Pe = 8.6$ and $\eta = 0.06$. The solid line represents the interface between regions 2 and 3 and AA' is the axis of symmetry. Maximum and average E_r in comparison of (a) and (b) is 0.09 and 2.5×10^{-3}, and between (c) and (d) is 0.5 and 0.03, respectively.
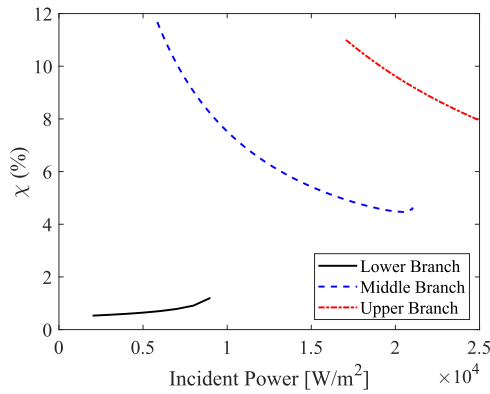
Fig. 8. Overall thermal efficiency of the device operating on respective branches of power response curves for $Pe = 4$.
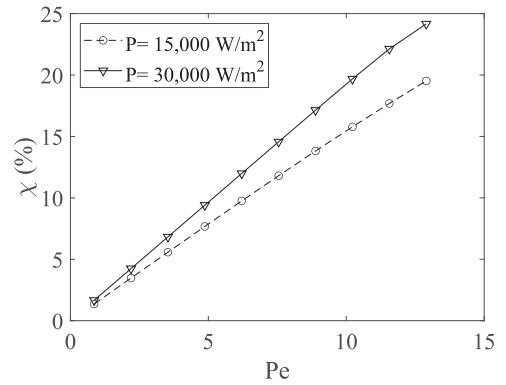
Fig. 9. Efficiency of the considered EM HX as a function of Pe when operated on the upper and middle branch for $\eta = 0.06$.

upper branches. From Fig. 9, slopes of the respective curves suggest that the rate at which P_{abs} increases with Pe is larger for the upper branch compared to the middle one. In other words, the rate at which convection heat transfer increases with Pe is larger on the upper branch. This explains why the upper branches undergo drastic temperature drop off with Pe. We expect that when Pe is large enough, upper branches would converge to the middle branch. Another observation is that with Pe, hysteresis on the upper branches keep diminishing, and the length of upper branch keep decreasing.

2) $Pe \sim o(1)$ and $Pe \sim o(\frac{1}{\eta})$ for $\eta = 0.05$: We now generate power response curves for $Pe \sim o(1)$ and $Pe \sim o(\frac{1}{\eta})$ for

$\eta = 0.05$. Response curves for this case are shown in Fig. 10. As found in the previous section, the convective heat transport within the fluid region causes reduction in temperature of middle and upper branches with Pe. As a result, hysteresis on the upper branch keep on diminishing with Pe as seen in Fig. 10(a). When Péclet numbers are moderate, i.e., $Pe = o(\frac{1}{\eta})$, from Fig. 10(b) we see that hysteresis is minimal, and transition between middle and upper branches is not as abrupt as compared to cases when $Pe \sim o(1)$. Next, we plot χ as a function of Pe in Fig. 11, when the steady-state solutions are on the middle and lower branches. To generate the plot, P_{av} is chosen such for $o(1) \leq Pe \leq o(\frac{1}{\eta})$, the steady-state solution are on the lower and middle branches
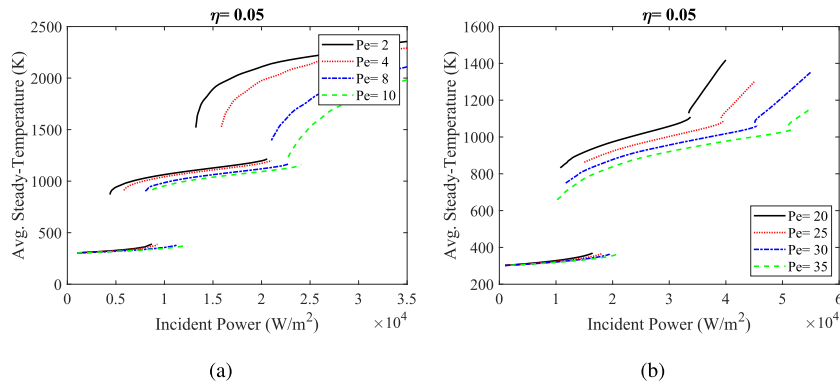
Fig. 10.   Stable branches of power response curves for different Péclet numbers produced using COMSOL Multiphysics model.
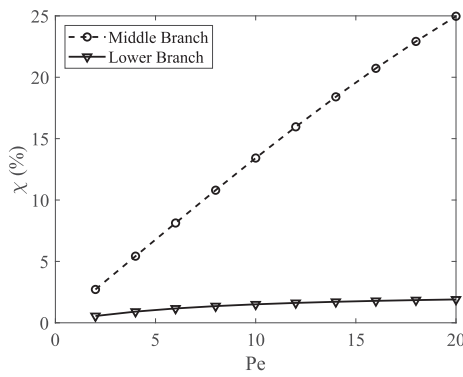
Fig. 11.   Overall thermal efficiency as a function of Pe when device is operated on lower and middle branches. Efficiencies for lower and middle branches are calculated for $P_{av} = 7000$ W/m^2 and $P_{av} = 15\,000$ W/m^2, respectively.

when initial temperature is maintained at 300 and 1000 K, respectively. We observe that the operation on the middle branch is more efficient (about 20%) compared to operation on the lower branch (about 1%). Another observation is that χ increases almost linearly with Pe when $o(1) \leq Pe \leq o(\frac{1}{\eta})$.

C. Local Onset of Thermal Runaway

In both cases (i.e., with and without fluid flow), we observe a hotspot in ceramic region when EM HX operates on the middle branch (see Figs. 5 and 7). In order to understand how hotspots are generated, we look at the transient behavior of temperatures in the ceramic. In Fig. 12, we plot transient snapshots of temperature profiles when a hotspot appears in the ceramic region for $P_{av} = 12\,000$ W/m^2 and $Pe = 0.3$. In Fig. 13 evolution of maximum and average temperatures T_{max} and T_{avg} with time is plotted for different incident powers P_{av} and Pe. To produce both figures, P_{av} and Pe are chosen such that steady-state solutions are on middle stable branch when initial temperature is maintained at 300 K. We explain the transient behavior in three stages.

Stage I: This region is before initiation of thermal runaway. Temperatures in region 3 are small and $\sigma_3 \approx 0.0004$. In that

case $|E_3|^2$ is large, but σ_3 is small such that the heat source $S|E_3|^2\sigma_3(T)$ is balanced by P_{abs}, thermal losses at the boundaries, and a small instantaneous temperature rise.

Stage II: In this region thermal runaway is observed. Instantaneous temperature profiles during this stage are shown in Fig. 12 for $P_{av} = 12\,000$ W/m^2 and $Pe = 4.3$. Transient T_{max} and T_{avg} for this case are shown in Fig. 13 (b). We observe that when $t = 64$ in Fig. 12 (a), maximum temperature reaches a critical value and thermal runaway is about to instigate. When $t = 66$, significant rise in maximum temperature (from 649 to 1651 K) takes place indicating initiation of thermal runaway and a local hotspot is observed as seen in Fig. 12 (b). At this critical moment, the EM losses in region 3, where the temperature is maximum, are large enough such that thermal losses at the boundaries and P_{abs} cannot balance the local heat source, which results in large instantaneous temperature rise and a local hotspot. Oscillations seen in transient T_{max} (in Fig. 13) during STAGE II indicate that mechanisms of heat generation (EM losses) and combined thermal losses (P_{abs} and losses at the boundaries) instantaneously try to dominate each other. When the hotspot in near the top boundary, P_{abs} is small as the hotspot is near the outlet. As the time progresses, thermal energy in the hotspot begins to dissipate toward the colder region in ceramic through conduction, and some energy is lost to the environment though thermal losses. As a result, the hotspot travels toward the negative *Y*-direction as seen from Fig. 12 (b)–(g). As the hotspot moves down, P_{abs} increases, as more time is available for the fluid to collect heat from the ceramic as it moves from inlet to outlet. Finally, the combined thermal losses begin to dominate heat generation and the thermal runaway stabilizes when $t = 120$ in Fig. 12 (h).

Stage III: During this stage, combined thermal losses balance the heat generation and equilibrium is achieved. As a result of the hotspot, fluid absorbs large thermal energy from the local heat source making EM HX more efficient when operated on the middle branch which is shown in Fig. 11.

The key observation from this study is that the thermal runaway is governed by local temperature. The slope of T_{max} at the critical point is much larger than the slope of T_{avg}. In other words, a rapid rise in local maximum results in a rise of average temperature during thermal runaway. This observation
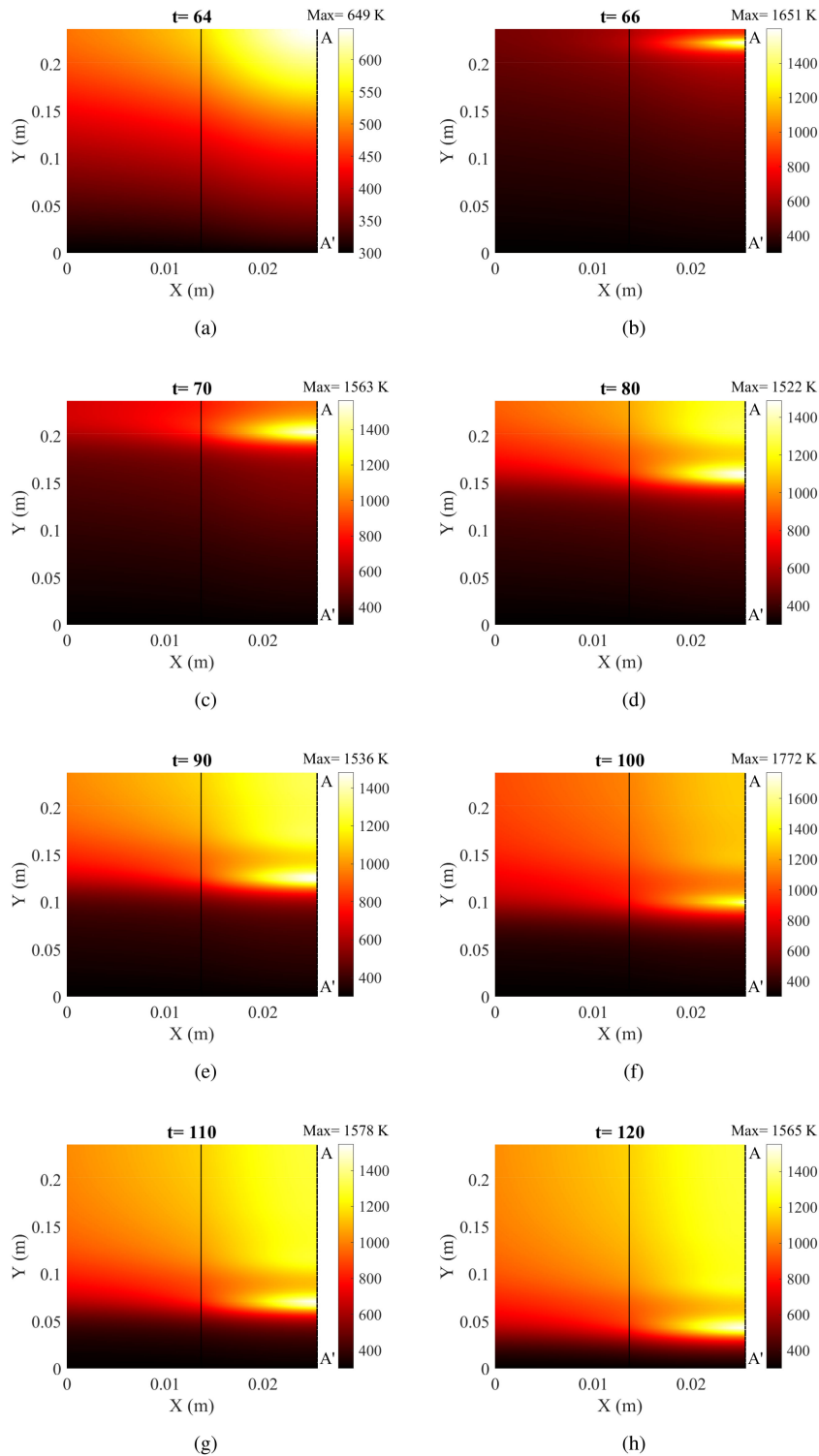
Fig. 12.   Transient evolution of the hotspot observed in STAGE *II* for $P_{av} = 12\,000$ W/m^2, $Pe = 4.3$. The solid line represents the interface between regions 2 and 3 and AA' is the axis of symmetry.

is consistent with results in [16] and [21]; as soon as the local maximum temperature reaches a critical value, thermal runaway initiates resulting in appearance of the hotspot. In our simulation for $Pe = 0$ and $Pe \neq 0$, we observe critical $T_{\max} \approx 650$ K.

D. Effect of Fluid Permittivity

Until now we discussed results when resonance criteria given by (2) is followed exactly. In this section, we relax the resonance criteria by varying fluid permittivity and keeping all other

(a)   (b)
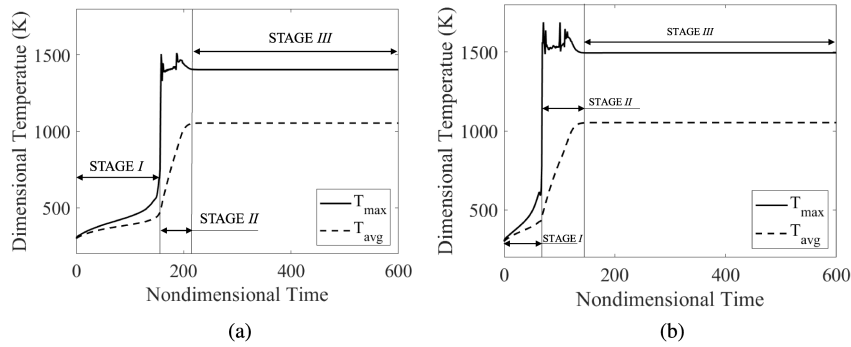
Fig. 13. Transient evolution of maximum and average temperatures T_{max} and T_{avg} given by COMSOL model when (a) $P_{av} = 9000$ W/m^2, $Pe = 0$ and (b)$P_{av} = 12\,000$ W/m^2, $Pe = 4.3$. Parameters P_{av} and Pe are chosen such that EM HX operates on the middle branch when initial temperature is 300 K. STAGE *I* is heating when there is no thermal runaway, STAGE *II* is stabilization of thermal runaway on the middle branch, and STAGE *III* is when steady-state is achieved.

(a)   (b)   (c)   (d)
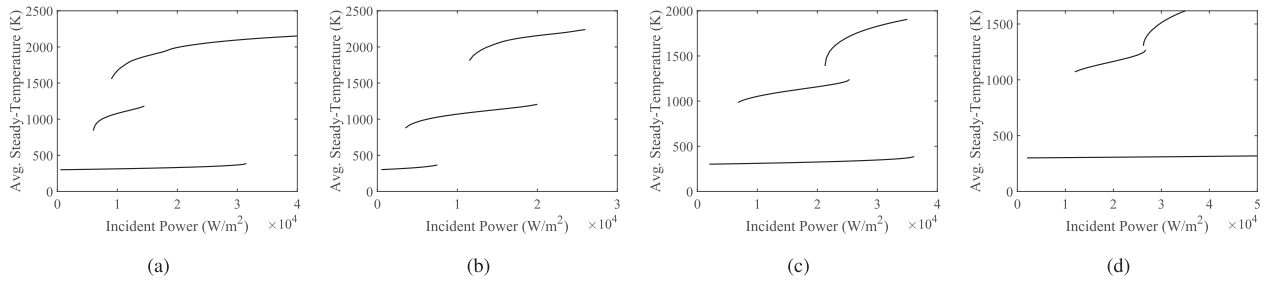
Fig. 14. Stable branches of power response curves for $Pe = 0$ and permittivity ratio. (a) $r = 6$. (b) $r = 6.76$ (perfect resonance). (c) $r = 7.6$. (d) $r = 8.6$.

(a)   (b)   (c)   (d)
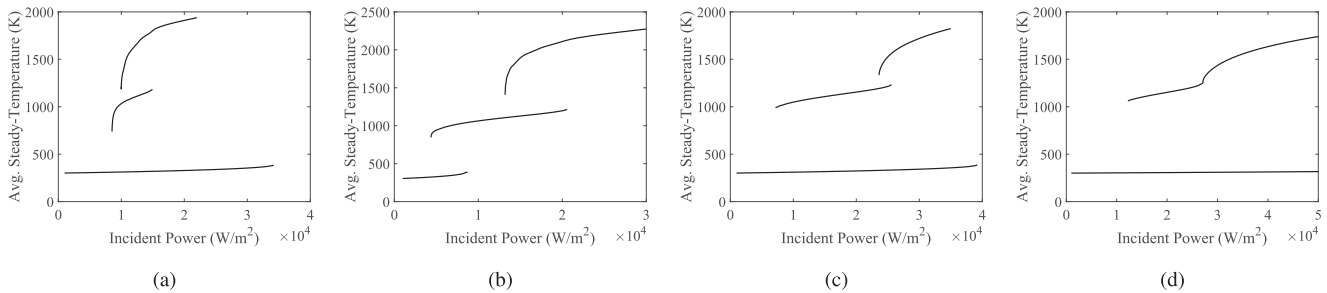
Fig. 15. Stable branches of power response curves for $Pe = 2$ and permittivity ratio. of $r = 6$ (a). (b) $r = 6.76$ (perfect resonance). (c) $r = 7.6$. (d) $r = 8.6$.

parameters constant. We define permittivity ratio as

$$r = \frac{\epsilon_{r_2}}{\epsilon_{r_3}}.$$

We keep ϵ_{r_3} constant and vary r. The perfect electric field resonance is achieved when $r = 6.76$. The goal here is to explore how the shape of the response curve changes in the neighborhood of $r = 6.76$.

For $Pe = 0$ and $Pe = 2$, power response curves for $r = 6$, $r = 6.76$, $r = 7.6$, and $r = 8.6$ are shown in Figs. 14 and 15, respectively. Although, we do not follow resonance criteria exactly, we still observe existence of middle branch in the neighborhood of $r = 6.76$. To understand how the middle branch behaves with permittivity ratio, we simulate response curves for

different r and Pe. We define length of the middle branch as the difference between powers at extreme points. Plot of the length of middle branches with r for different Pe is shown in Fig. 16. We see that the length of middle branches slowly starts to increase we approach the reference $r = 6.76$, and keeps on increasing until it reaches to maximum at $r = 7.4$. The plot in Fig. 16 gives an estimate on the ranges of r within which we have three distinct stable branches. As we start to move away from the ranges shown in the plot, the middle branch merges into the upper branch as seen from Figs. 14(d) and 15(d), and eventually acquires a typical S-shaped power response curve as shown in Fig. 2(a) if permittivity ratio is increased even further. In that case, only two stable branches exists; the lower branch (~ 300 K) and the upper branch (~ 2500 K). These observations
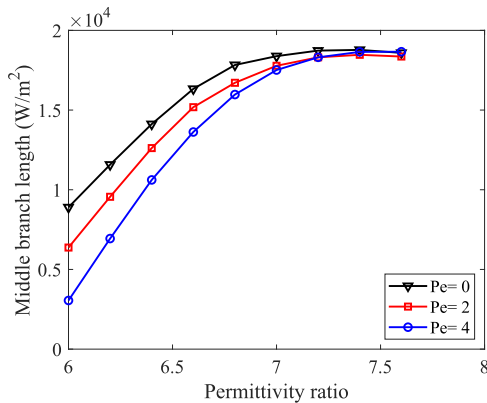
Fig. 16.   Length of the middle branch as a function of permittivity ratio r.

are inline with results discussed in [26] and [27]. These papers, for the no flow case, report that the length of the middle branch first increases and then decreases with permittivity ratio.

The idea of resonance-based control over thermal runaway relies on the existence of the middle branch. We have demonstrated that the middle branch exists, as long as permittivity variation is within roughly 10% of the reference $r = 6.76$ as seen in Fig. 16 for $Pe \sim o(1)$.

IV. CONCLUSION

In this article, we presented a numerical model produced in COMSOL Multiphysics which describes the operation of a triple-layer EM HX with plane Poiseuille flow. The model is validated by comparing steady-state electric field and temperature profiles with the ones produced by another model using an IMEX finite-difference scheme. Because of the electric field resonance in the lossy region we found that power response curve stet is a double S-curve when $Pe \sim o(1)$ and $Pe \sim o(\frac{1}{\eta})$. We have found that EM HX operating on the middle branch are more efficient (about 20%) compared to those operating on the lower branch (about 1.5%) when $Pe \sim o(\frac{1}{\eta})$.

From the comparison of power response curves for different Pe, we observe that the average temperatures of upper and middle stable branches keep dropping as Pe is increased. Large convection heat transfer between the fluid and the ceramic causes the upper branches undergo drastic reduction in temperatures compared to the middle and lower branches. When Pe is sufficiently large around $o(\frac{1}{\eta})$, we observe hysteresis on the upper branch diminishes.

We have described the transient behavior of the thermal runaway in triple-layer EM HX. Results confirm that thermal runaway instigates as soon as the local maximum temperature reaches a critical value. The EM losses in region 3, at the point where the temperature is maximum, are large enough such that thermal losses at the boundaries and convection between coolant and the ceramic cannot balance the local heat source, which results in large instantaneous temperature rise and a local hotspot. As the time progresses, the hotspot travels toward the bottom boundary allowing fluid to collect thermal energy from the local heat source. The hotspot in ceramic region causes

an EM HX to operate more efficiently on the middle branch. When thermal losses at the boundaries and power absorbed by fluid balance the local heat source, steady state is achieved and thermal runaway stabilizes on the middle branch.

We also investigated cases where we vary permittivity of the fluid region, keeping all other parameters fixed. We found that middle branch exists for $Pe \sim o(1)$ when the variations in fluid permittivity are roughly within 10% of the reference value.

REFERENCES

[1] A. K. Datta and R. C. Anantheswaran, *Handbook Microwave Technology for Food Application*, Boca Raton, FL, USA: CRC Press, 2001.

[2] M. Willert-Porada, Ed., *Advances in Microwave Radio Frequency Processing*, Berlin, Germany: Springer, 2006.

[3] N. Leadbeater, *Microwave Heating as a Tool for Sustainable Chemistry*, Boca Raton, FL, USA: CRC Press, 2010.

[4] J. Aguilar-Garib, "Thermal microwave processing of materials," in *Advances in Induction and Microwave Heating of Mineral and Organic Materials*, C. Grundas, Ed., Rijeka, Croatia: InTech, 2011, pp. 243–268.

[5] S. Chandrasekaran, S. Ramanathan, and T. Basak, "Microwave materials processing — A review," *AIChE J.*, vol. 58, no. 2, pp. 330–363, 2012.

[6] S. Singh, D. Gupra, V. Jain, and A. Sharma, "Microwave processing and applications of manufacturing industry: a review," *Mater. Manuf. Process.*, vol. 30, no. 1, pp. 1–29, 2015.

[7] K. L. Parkin, L. D. DiDomenico, and F. E. Culick, "The microwave thermal thruster concept," *Proc. 2nd Int. Symp. Beamed Energy Propulsion*, 2004, pp. 418–429.

[8] G. A. Landis, "Beamed energy propulsion for practical interstellar flight," *J. Brit. Interplanetary Soc.*, vol. 52, pp. 420–423, 1999.

[9] J. C. Coopersmith and E. Davis, "A strategic roadmap for commercializing low-cost beamed energy propulsion launch systems," in *Proc. AIAA SPACE*, 2016, Art. no. 5555.

[10] A. Jamar, Z. Majid, W. Azmi, M. Norhafana, and A. Razak, "A review of water heating system for solar energy applications," *Int. Commun. Heat Mass Transfer*, vol. 76, pp. 178–187, 2016.

[11] W. C. Brown and E.E. Eves, "Beamed microwave power transmission and its application to space," *IEEE Trans. Microw. Theory Techn.*, vol. 40, no. 6, pp. 1239–1250, Jun. 1992.

[12] J. N. Benford and R. Dickinson, "Space propulsion and power beaming using millimeter systems," *Intense. Microw. Pulses III*, vol. 2557, 1995, pp. 179–192.

[13] J. N. Benford, "Space applications of high-power microwaves," *IEEE Trans. Plasma Sci.*, vol. 36, no. 3, pp. 569–581, Jun. 2008.

[14] B. Jawdat *et al.*, "Composite ceramics for power beaming," in *Proc. IEEE Wireless Power Transfer Conf.*, 2017, pp. 1–4.

[15] B. W. Hoff *et al.*, "Millimeter wave interactions with high temperature materials and their applications to power beaming," in *Proc. 52nd IMPI's Microw. Power Symp.*, Long Beach, CA, Jun. 2018, pp. 82–83.

[16] A. A. Mohekar, J. M. Gaone, B. S. Tilley, and V. V. Yakovlev, "A 2D coupled electromagnetic, thermal and fluid flow model: Application to layered microwave heat exchangers," in *Proc. IEEE MTT-S Int. Microw. Symp.*, Philadelphia, PA, USA, Jun. 2018, pp. 1389–1392.

[17] A. A. Mohekar, B. S. Tilley, and V. V. Yakovlev, "A 2D model of a triple layer electromagnetic heat exchanger with porous media flow," in *Proc. IEEE MTT-S Int. Microw. Symp.*, Boston, MA, USA, Jun. 2019, pp. 59–62.

[18] A. A. Mohekar, B. S. Tilley, and V. V. Yakovlev, "Plane wave irradiation of a layered system: Resonance-based control over thermal runaway," in *Proc. 17th Int. Conf. Microw. and High Freq. Heating*, Valencia, Spain, Sep. 2019, pp. 292–300.

[19] P. Kumi, S. A. Martin, V. V. Yakovlev, M. S. Hilario, B. W. Hoff, and I. M. Rittersdorf, "Electromagnetic-thermal model of a millimeter-wave heat exchanger based on an AlN:Mo susceptor," *COMPEL - Int. J. Comput. Math. Elect. Electron. Eng.*, vol. 39, no. 2, pp. 481–496, 2020.

[20] J. M. Hill and M. J. Jennings, "Formulation of model equations for heating by microwave radiation," *Appl. Math. Modelling*, vol. 17, no. 7, pp. 369–379, 1993.

[21] V. V. Yakovlev, S. M. Allan, M. L. Fall, and H. S. Shulman, "Computational study of thermal runaway in microwave processing of zirconia," in *Microwave and RF Power Applications*, J. Tao, Ed. Toulouse, France: Cépaduès, 2011, pp. 303–306.

[22] X. Wu, Experimental theoretical study of microwave heating thermal runaway materials, Ph.D. dissertation, Dept. Mech. Eng., Virginia Polytechnic Inst. State Univ., Blacksburg, VA, USA, 2002.

[23] X. Wu, J. Thomas Jr, and W. A. Davis, "Control of thermal runaway in microwave resonant cavities," *J. Appl. Phy.*, vol. 92, no. 6, pp. 3374–3380, 2002.

[24] G.A. Kriegsmann, "Themal runaway in microwave heated ceramic: A one-dimensional model," *J. Appl. Phy.*, vol. 71, no. 4, pp. 1960–1966, 1992.

[25] J. A. Pelesko, G. A. Kriegsmann, "Microwave heating of ceramic laminates," *J. Eng. Math.*, vol. 32, no. 1, pp. 1–18, 1997.

[26] J. M. Gaone, B. S. Tilley, and V. V. Yakovlev, "Permittivity-based control of thermal runaway in a triple-layer laminate," in *Proc. IEEE MTT-S Int. Microw. Symp.*, Honolulu, HI, Jun. 2017, pp. 459–462.

[27] J. M. Gaone, B. S. Tilley, and V. V. Yakovlev, "Electromagnetic heating control via high-frequency resonance of a triple-layer laminate," *J. Eng. Math.*, vol. 114, no. 1, pp. 65–86, 2019.

[28] S. J. Ruuth, "Implicit-explicit methods for reaction-diffusion problems in pattern formation," *J. Math. Biol.*, vol. 34, no. 2, pp. 148–176, 1995.

[29] P. M. Meaney, C. J. Fox, S. D. Geimer, and K. D. Paulsen, "Electrical characterization of glycerin: water mixtures: Implications for use as a coupling medium in microwave tomography," *IEEE Trans. Microw. Theory Techn.*, vol. 65, no. 5, pp. 1471–1478, May 2017.

[30] Glycerine Producers' Association, *Physical Properties of Glycerine its Solutions*, New York, NY, USA: Glycerine Producers' Assoc., 1963.

[31] G. I. Taylor, "Dispersion of soluble matter in solvent flowing slowly through a tube," *Proc. Roy. Soc. London, Ser. A, Math. Phys. Sci.*, vol. 219, no. 1137, pp. 186–203, 1953.

[32] Y. Saad, *Iterative Methods for Sparse Linear Syst.*, Philadelphia, PA, USA: SIAM, 2003.

[33] W. H. Press, B. P. Flannery, S. A. Teukolsky, and W. T. Vetterling, *Numerical Recipes*, New York, NY, USA: Cambridge Univ. Press, 1989.

[34] S. Mazumder, *Numerical Methods for Partial Differential Equations: Finite Difference and Finite Volume Methods*, London, U.K.: Academic, 2015.

[35] M. N. Sadiku, *Numerical Techniques Electromagnetics With MATLAB*, Boca Raton, FL, USA: CRC Press, 2011.

[36] Y. S. Wong and G. Li, "Exact finite difference schemes for solving Helmholtz equation at any wavenumber," *Int. J. Numer. Anal. Model., Ser. B*, vol. 2, no. 1, pp. 91–108, 2011.

[37] D. Salvi, D. Boldor, G. Aita, and C. Sabliov, "COMSOL Multiphysics model for continuous flow microwave heating of liquids," *J. Food Eng.*, vol. 104, no. 3, pp. 422–429, 2011.

[38] D. Salvi, D. Boldor, J. Ortego, G. Aita, and C. Sabliov, "Numerical modeling of continuous flow microwave heating: a critical comparison of COMSOL and ANSYS," *J. Microw. Power Electromagn. Energy*, vol. 44, no. 4, pp. 187–197, 2010.

Ajit A. Mohekar received the B.E. degree from the Savitribai Phule Pune University, Pune, India, in 2015 and the M.S. degree from Worcester Polytechnic Institute, in 2018, both in mechanical engineering, where he is currently working toward the Ph.D. degree in mechanical engineering.

His research interests include modeling multiphysics problems involving electromagnetics, fluid dynamics, and heat transfer phenomena.

Mr. Mohekar was the recipient of the Best Student Poster Award of the "Electromagnetic Fields in Materials Synthesis" Symposium at the Materials Research Society (MRS) Fall 2018 meeting in Boston, MA, USA.

Burt S. Tilley received the B.S degree in electrical engineering and the B.A. degree in modern languages from the University of Massachusetts Lowell, Lowell, MA, USA, in 1988, and the Ph.D. degree in applied mathematics, focusing on interfacial fluid dynamics from Northwestern University, Evanston, IL, USA, in 1994.

He received a tenure-track position with the Mathematical Sciences Department at the New Jersey Institute of Technology, with a focus on electrohydrodynamics in thin liquid films and microwave-enhanced chemical vapor infiltration applications, and a North Atlantic Treaty Organization (NATO)/National Science Foundation (NSF) Postdoctoral Research Fellowship with the Hydrodynamics Laboratory at Ecole Polytechnic in Palaiseau, France. In 2001, he was the first permanent Mathematician hired on the faculty with the then new Franklin W. Olin College of Engineering, Needham, MA, USA. In 2009, he moved to his current position with Worcester Polytechnic Institute, Worcester, MA, USA, and has been the Director of the Center for Industrial Mathematics and Statistics (CIMS), since 2013. He has received funding for his work from the NSF, Air Force Office of Scientific Research, and other industrial and governmental agencies.

Vadim V. Yakovlev (Senior Member, IEEE) received the M.Sc. degree in radio physics and electronics from Saratov State University, Saratov, Russia, in 1979, and the Ph.D. degree in radio physics from the Institute of Radio Engineering and Electronics (IRE), Russian Academy of Sciences (RAS), Moscow, Russia, in 1991.

From 1984 to 1996, he was a Junior Research Scientist, Research Scientist, and Senior Research Scientist with IRE RAS. In 1993, he was a Visiting Researcher with the Centre "Les Renardières," Electricité de France, Paris, France. In 1996, he joined the Department of Mathematical Sciences, Worcester Polytechnic Institute (WPI), Worcester, MA, USA, as a North Atlantic Treaty Organization (NATO)/National Science Foundation (NSF) Fellow. He has been with this Department since then, where he is currently an Associate Research Professor. He is a Head of the Industrial Microwave Modeling Group, which he established in 1999, as a division of Center for Industrial Mathematics and Statistics, WPI. He has authored nearly 200 papers in peer-reviewed journals and conference proceedings. Funding sources of his research include the National Science Foundation (NSF), Air Force Research Laboratory (AFRL), Air Force Office of Scientific Research (AFOSR), and EADS (currently Airbus Group). His current research interests include multiphysics modeling, microwave power engineering, broadband and multiband antennas, microwave imaging, and machine-learning optimization.

Dr. Yakovlev is a Fellow of International Microwave Power Institute (IMPI), a member of the Association for Microwave Power in Europe for Research and Education (AMPERE), and Member of the Massachusetts Institute of Technology (MIT) Electromagnetics Academy In 2013, he served as Chair of the Technical Program Committee for the 47th IMPI Microwave Power Symposium. Since 2010, he has been a member and Subcommittee Chair of the IEEE Microwave Theory and Techniques Society (MTT-S) International Microwave Symposium (IMS) Technical Paper Review Committee (TPRC). He is the Founder of a series of international interdisciplinary seminars, "Computer Modeling in Microwave Power Engineering" held annually from 2000 to 2016 and biannually, since 2017. In 2007, he was a Guest Editor for the "Special Issue on Modeling in Microwave Power Engineering" of the *Journal of Microwave Power and Electromagnetic Energy*. He has been Reviewer for several journals and member of program committees of several conferences.